Anomalous isotopic predissociation in the F 3 u (v=1) state of O 2

B. R. Lewis, S. T. Gibson, J. P. England, G. Stark, and J. B. West

Citation: The Journal of Chemical Physics **116**, 3286 (2002); doi: 10.1063/1.1436106
View online: http://dx.doi.org/10.1063/1.1436106
View Table of Contents: http://scitation.aip.org/content/aip/journal/jcp/116/8?ver=pdfcov
Published by the AIP Publishing

Anomalous isotopic predissociation in the $F\,^3\Pi_u(v=1)$ state of O_2

B. R. Lewis, S. T. Gibson, and J. P. England[a)]
Research School of Physical Sciences and Engineering, The Australian National University, Canberra, ACT 0200, Australia

G. Stark
Department of Physics, Wellesley College, Wellesley, Massachusetts 02481

J. B. West
Daresbury Laboratory, Warrington, WA4 4AD, United Kingdom

(Received 2 November 2001; accepted 27 November 2001)

Using a tunable, narrow-bandwidth vacuum-ultraviolet source based on third-harmonic generation from excimer-pumped dye-laser radiation, the $F\,^3\Pi_u \leftarrow X\,^3\Sigma_g^-(1,0)$ photoabsorption cross sections of $^{16}O_2$ and $^{18}O_2$ have been recorded in high resolution. Rotational analyses have been performed and the resultant $F(v=1)$ term values fitted to the $^3\Pi$ Hamiltonian of Brown and Merer [J. Mol. Spectrosc. **74**, 488 (1979)]. A large rotationless isotope effect is observed in the $F(v=1)$ predissociation, wherein the Lorentzian linewidth component for $^{18}O_2$ is a factor of ~50 smaller than the corresponding $^{16}O_2$ linewidth. This effect, a consequence of the nonadiabatic rotationless predissociation mechanism, is described using a coupled-channel treatment of the strongly Rydberg-valence-mixed $^3\Pi_u$ states. Significant J, e/f-parity, and sublevel dependencies observed in the isotopic $F(v=1)$ rotational widths are found to derive from an indirect predissociation mechanism involving an accidental degeneracy with the $E\,^3\Sigma_u^-(v=3)$ level, itself strongly predissociated by $^3\Sigma_u^-$ Rydberg-valence interactions, together with **L**-uncoupling (rotational) interactions between the Rydberg components of the F and E states. Transitions into the $E(v=3)$ level are observed directly for the first time, specifically in the $^{18}O_2$ spectrum. © *2002 American Institute of Physics.* [DOI: 10.1063/1.1436106]

I. INTRODUCTION

Perturbations in molecular spectra lead to a wide range of interesting effects.[1] In particular, strong Rydberg-valence interactions can produce anomalous behavior in the vibrational, rotational, and isotopic dependencies of line positions, intensities, predissociation widths, and asymmetries.

In the case of O_2, for example, interactions between the $\pi_u^3\pi_g^3\,^3\Sigma_u^-$ valence state and the $3p\pi_u\,^3\Sigma_u^-$ Rydberg state[2] ($H^{el}\approx 4000\ cm^{-1}$) control the bulk of the ground-state spectral structure and predissociation dynamics in the 1170–1400-Å (71 400–85 500-cm^{-1}) region. Anomalous isotopic shifts and anomalous isotopic dependencies of predissociation linewidth and line-shape asymmetry have been reported[3–5] for the $E\,^3\Sigma_u^- \leftarrow X\,^3\Sigma_g^-(0,0)$ transition of O_2, near 1245 Å, where the E state is the upper adiabatic state formed by the avoided crossing between the Rydberg and valence states of $^3\Sigma_u^-$ symmetry.

The $\pi_g\sigma_u\,^3\Pi_u$ valence and $\pi_g 3p\sigma_u\,^3\Pi_u$ Rydberg states of O_2 are known to interact even more strongly than the $^3\Sigma_u^-$ states[2] ($H^{el}\approx 7000\ cm^{-1}$) and might be expected to exhibit similar effects. Indeed, anomalous vibrational spacings have been reported in the $F\,^3\Pi_u$ state of O_2,[6] where the F state is the upper adiabatic (double-well) state formed by interactions among the valence, $3p$, and $4p$ Rydberg states of $^3\Pi_u$ symmetry. In addition, wildly differing intensity ratios have been observed for the (0,0) and (1,0) bands of the $F\,^3\Pi_u - X\,^3\Sigma_g^-$ system in single- and three-photon excitation, attributed to the effects of the Rydberg-valence interaction.[7]

In Fig. 1 of the review of the $^3\Pi_u \leftarrow X\,^3\Sigma_g^-$ transitions of O_2, by England *et al.*,[6] there is an apparent isotopic intensity anomaly, hitherto unexplained. In particular, the $F \leftarrow X(1,0)$ band of $^{18}O_2$, near 1153 Å (86 730 cm^{-1}), appears considerably weaker than the corresponding band of $^{16}O_2$ and exhibits apparent subband intensity anomalies. In this work, with the aid of high-resolution measurements of the photoabsorption cross section for the $F \leftarrow X(1,0)$ band of $^{18}O_2$, we show that the apparent intensity anomaly is a result of anomalous isotopic dependence in the *predissociation* of $F(v=1)$, together with the effects of inadequate instrumental resolution in previous experiments.[6] Spectroscopic parameters are determined for the $F(v=1)$ levels of $^{16}O_2$ and $^{18}O_2$ and the isotopic pattern of predissociation is explained with the aid of coupled-channel Schrödinger equation (CSE) models of the $^3\Pi_u$ and $^3\Sigma_u^-$ Rydberg-valence interactions.

II. EXPERIMENTAL METHOD

Photoabsorption cross sections were measured for the $F \leftarrow X(1,0)$ bands of $^{16}O_2$ and $^{18}O_2$ near 1153 Å using tunable, narrow-bandwidth, coherent vacuum-ultraviolet (vuv) radiation obtained by third-harmonic generation in a nonlinear medium.[8] The apparatus was similar to that employed in the measurement of CO $A \leftarrow X$ and $B \leftarrow X$ oscillator strengths.[9,10] Briefly, a XeCl excimer laser (3080 Å, 10 Hz)

[a)]Deceased, 5 December 2000.

was used to pump a dye laser (*p*-terphenyl in dioxane) equipped with an intracavity étalon. The near-uv output of the dye laser (~3460 Å) was focused into a cell containing Kr, at pressures ranging from 40 to 100 Torr, adjusted to optimize the phase matching for the third-harmonic-generation process. The generated radiation was then passed through a 0.2-m scanning vuv monochromator in order to remove the fundamental near-uv radiation. The bandwidth of the resulting vuv radiation was estimated to be $\sim 0.15\ cm^{-1}$ full width at half maximum (FWHM) by fitting the absorption line shapes of narrow, near-Doppler-broadened low-rotation lines near the $^{18}O_2$ $F \leftarrow X(1,0)$ subband heads. A similar value resulted from the fitting of Doppler-broadened lines in the nearby CO $B \leftarrow X(0,0)$ band. The known wavelengths for these CO lines,[11] which lie at the short-wavelength limit of the $F \leftarrow X(1,0)$ scans, were also used to provide absolute calibration of the dye-laser wavelength scale, the linearity of which was calibrated using the known ground-state combination differences for $^{18}O_2$.[12]

vuv radiation leaving the monochromator was divided into two beams by a slotted Al beam splitter, the reflected beam serving as a monitor of the laser intensity, while the transmitted beam passed through a LiF-windowed, temperature-controllable absorption cell before being detected. Both beams were detected by solar-blind photomultipliers. Samples of O_2 (BOC 99.99% O_2, natural isotopic abundance; and ICON 97 at. % ^{18}O) were used at pressures between 0.01 and 1.0 Torr, chosen to produce transmittances at line centers between 30% and 70%. In the case of measurements on normal O_2, the dye-laser intracavity étalon was not employed, resulting in an effective resolution of $\sim 0.5\ cm^{-1}$ FWHM. Since, as will be seen in Sec. IV, the $^{16}O_2$ linewidths are much larger than those for $^{18}O_2$, this did not result in any instrumental degradation of the $^{16}O_2$ spectra. Absolute O_2 pressures in the absorption cell were monitored by a variable-capacitance manometer. Measurements were performed both at room temperature (298 K) and liquid nitrogen (LN_2) temperature (effective cell temperature 79 K).

Output pulses from the monitor and detector photomultipliers were processed by a boxcar system, with averaging over 100 laser shots. For each datum point, the averaged detector signal was divided by the averaged monitor signal in order to account for the shot-to-shot fluctuations inherent in the generated vuv signal. Before and after each absorption scan, empty-cell signals were recorded: absolute cell transmittances were determined by dividing the full-cell ratios (detector/monitor) by the empty-cell ratios for each datum point. The resulting signal-to-noise ratio in a typical scan was about 40:1. The level of amplified spontaneous emission in the generated vuv radiation was expected to be less than 3%, as determined from measurements on the Doppler-broadened lines of the CO $B \leftarrow X(0,0)$ system.[10] Absolute photoabsorption cross sections (systematic uncertainty ~3%, statistical uncertainty typically ~5%) were determined from the corrected transmittances using the Beer–Lambert law.

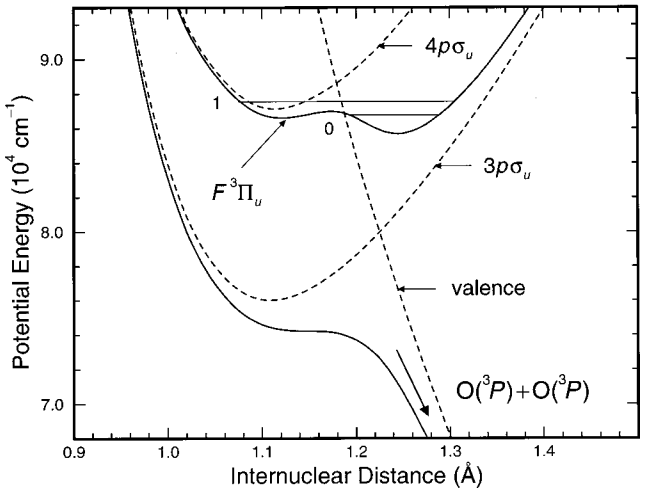

FIG. 1. Diabatic (dashed curves) and adiabatic (solid curves) potential-energy curves for the interacting Rydberg and valence $^3\Pi_u$ states of O_2. The energy scale is referred to the minimum in the $X\,^3\Sigma_g^-$ potential (not shown). The lowest two vibrational levels of the *F* state for $^{16}O_2$ are also indicated.

III. THEORETICAL METHOD

As mentioned in Sec. I, the *F* state of O_2 is a mixed state involving the bound $\pi_g np\sigma_u\ ^3\Pi_u$ Rydberg states with $n=3$ and 4, and the $\pi_g\sigma_u\ 1\ ^3\Pi_u$ repulsive valence state. Diabatic potential-energy curves for these states are shown in Fig. 1 (dashed curves).[7,13] The molecular-orbital (MO) configurations of the Rydberg and valence states differ only by a single orbital. In the diabatic basis, there are strong Rydberg-valence interactions,[1] leading to the adiabatic potential-energy curves[7,13] in Fig. 1 (solid curves), which show strongly avoided crossings. In an adiabatic picture, the lowest Rydberg-valence interaction is an example of Rydbergization, the $3\sigma_u$ valence MO becoming the $3p\sigma_u$ Rydberg MO as the internuclear distance *R* decreases.[1] The double-minimum adiabatic potential in Fig. 1 is associated with the $F\,^3\Pi_u$ state. It should be noted that the first two vibrational levels in the *F*-state potential are of inherently different character, with $F(v=0)$ located principally in the outer well, while $F(v=1)$ spans both wells.

While the adiabaticity parameter[14] for the $n=3$ Rydberg-valence crossing, $\zeta=2.9$,[6] is significantly greater than unity, implying essentially adiabatic behavior for the *F* state, it is, nevertheless, the residual nonadiabatic coupling between the adiabatic states that is primarily responsible for the predissociation of the *F*-state levels. This type of predissociation is not readily treatable using perturbative techniques, but is amenable to a CSE treatment of the interacting Rydberg and valence states.[15–17] Here, for computational convenience, we employ a *diabatic* basis of interacting Rydberg and valence states, since the corresponding electronic properties can be expected to change smoothly with *R*.

Details of the CSE method employed can be found in Ref. 18. Briefly, the cross section, in cm^2, for single-photon absorption from a given rovibrational level of an initial uncoupled electronic state into the *n* coupled states *k*, at an energy *E*, and with rotation *J* is given by

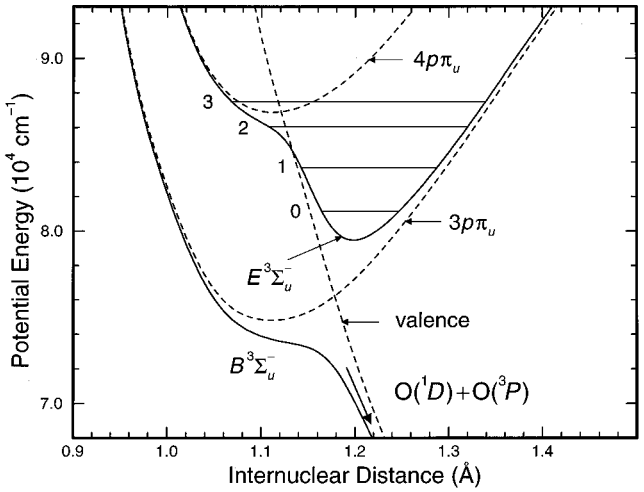

FIG. 2. Diabatic (dashed curves) and adiabatic (solid curves) potential-energy curves for the interacting Rydberg and valence $^3\Sigma_u^-$ states of O_2. As in Fig. 1, the energy scale is referred to the minimum in the $X\,^3\Sigma_g^-$ potential (not shown). The lowest four vibrational levels of the E state for $^{16}O_2$ are also indicated.

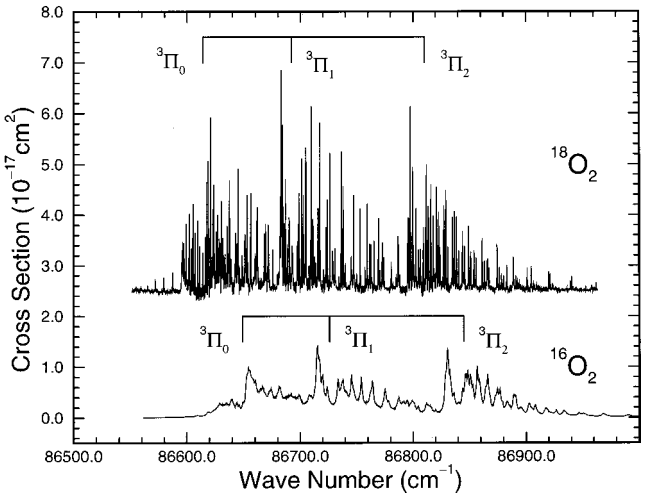

FIG. 3. Overall experimental room-temperature photoabsorption cross sections for the $F\,^3\Pi_u \leftarrow X\,^3\Sigma_g^-(1,0)$ bands of isotopic O_2, highlighting a strong isotopic effect in the apparent linewidths. Origins for the $\Omega'=0$, 1, and 2 subbands are indicated. The $^{18}O_2$ cross section has been raised by 2.5×10^{-17} cm^2, for clarity.

$$\sigma_{EJ;v''J''}=1.23\times10^{-23}g\,\nu|\langle\boldsymbol{\chi}_{EJ}(R)|\mathbf{M}|\chi_{v''J''}(R)\rangle|^2. \quad (1)$$

In Eq. (1), ν is the transition energy, in cm^{-1}, g is a degeneracy factor, $\boldsymbol{\chi}_{EJ}(R)$ is the coupled-channel radial wave-function matrix, $\chi_{v''J''}(R)$ is the radial wave function of the initial state, and the transition matrix elements are in atomic units. The elements of the $n\times1$ rotronic (rotational-electronic) transition-moment vector $\mathbf{M}$ are the products of appropriately normalized electronic transition moments $\mathcal{M}_k(R)$ and rotational matrix elements of the direction-cosine operator. The coupled-channel radial wave-function matrix $\boldsymbol{\chi}_{EJ}(R)$ is the solution of the diabatic-basis coupled Schrödinger equations, expressed in matrix form,

$$\left\{\mathbf{I}\frac{d^2}{dR^2}+\frac{2\mu}{\hbar^2}[E\mathbf{I}-\mathbf{V}(R)-\mathbf{V}^{\rm rot}(R)]\right\}\boldsymbol{\chi}_{EJ}(R)=0. \quad (2)$$

In Eq. (2), μ is the molecular reduced mass, $\mathbf{I}$ is the identity matrix, $\mathbf{V}(R)$ is the symmetric $n\times n$ diabatic potential matrix, the diagonal elements of which are the diabatic electronic potential-energy curves $V_k(R)$, and $\mathbf{V}^{\rm rot}(R)$ is a diagonal matrix with elements given by matrix elements of the rotational part of the molecular Hamiltonian. The couplings between the interacting electronic states are given by the off-diagonal elements of $\mathbf{V}(R)$, which, for example, may contain the effects of electrostatic, rotational, and spin-orbit interactions.

If the electronic wave functions are expressed in the Hund's case (a) e/f-parity basis,[1] then the only nonzero elements $\mathcal{M}_k(R)$ arise from dipole-allowed transitions between case (a) basis states. For a specific temperature, the total cross section can be expressed as the sum of cross sections into the upper-state e and f levels, each of which is calculated separately as a Boltzmann average of Eq. (1) over the initial distribution of ground-state vibrational, rotational, and fine-structure levels. In this work, however, we restrict ourselves to representative single-line cross-section calculations for specific $J=J''$.

A basic three-state diabatic CSE model,[7,13] adapted from the six-state model of England *et al.*,[6] is used here to describe the interacting $^3\Pi_u$ states. In this model,[7,13] the diabatic Rydberg and valence $^3\Pi_u$ potential-energy curves of Fig. 1 form the diagonal elements of the potential matrix $\mathbf{V}(R)$, the only nonzero off-diagonal elements of which are the Rydberg-valence couplings (taken to be R-independent) of 7034 and 3403 cm^{-1}, respectively, for the $3p\sigma_u$ and $4p\sigma_u$ states. The model diabatic $^3\Pi_u \leftarrow X\,^3\Sigma_g^-$ electronic transition moments are taken from Ref. 13. **S**-uncoupling interactions between the $^3\Pi_{u\Omega}$ sublevels are ignored, separate calculations for each Ω being performed by shifting the potential-energy curves in energy to reproduce the diagonal spin–orbit splitting. This approach should be satisfactory for low J, where the $^3\Pi_u$ states approach Hund's case (a) angular-momentum coupling.

Cross sections for excitation into the coupled $^3\Pi_u$ states of isotopic O_2 were calculated in the energy range of the $F\leftarrow X(1,0)$ band using Eqs. (1) and (2) with these diabatic model parameters. The diabatic coupled-channel radial wave functions $\boldsymbol{\chi}_{EJ}(R)$, normalized according to the method of Mies,[15] were obtained by solving Eq. (2) using the renormalized Numerov method of Johnson.[19] The ground-state vibrational wave function $\chi_{v''J''}(R)$ was calculated using a Rydberg–Klein–Rees potential-energy curve for the $X\,^3\Sigma_g^-$ state constructed from the spectroscopic constants of Cosby.[20] CSE estimates of the predissociation linewidths were obtained by fitting Lorentzian profiles to the computed cross sections.

As we show in Sec. IV B, the rotational part of the F-state predissociation cannot be explained by the nonadiabatic $^3\Pi_u$ mechanism alone, and it becomes necessary to consider indirect $^3\Sigma_u^-$ predissociation channels. In the energy region of $F(v=1)$, the $E\,^3\Sigma_u^-$ state of O_2 is also a mixed

TABLE I. Term values for the $F\,^3\Pi_{u\Omega}(v=1,J)$ levels of isotopic O_2, in cm^{-1}.

	$^{16}O_2$[a,b]			$^{18}O_2$[a,c]		
J	$\Omega=0$	$\Omega=1$	$\Omega=2$	$\Omega=0$	$\Omega=1$	$\Omega=2$
0	86 652.2[d]			86 616.50		
1	86 655.1[e]	86 732.8[d]		86 618.99	86 697.61	
2	86 661.2	86 739.1	86 851.5	86 624.64	86 703.19	86 815.78
3	86 670.0	86 748.9	86 861.2	86 632.54	86 711.86	86 824.36
4	86 682.3	86 761.0	86 874.0	86 643.67	86 722.86	86 835.79
5	86 697.0	86 777.4	86 890.1	86 657.01	86 737.49	86 850.08
6	86 715.3	86 795.5	86 909.4	86 673.58	86 753.71	86 867.21
7	86 736.0	86 818.9	86 931.8	86 692.38	86 774.40	86 887.23
8	86 760.2[d]	86 842.6	86 957.5	86 714.31	86 795.87	86 910.03
9	86 787.9	86 873.0	86 986.5	86 738.57	86 822.66	86 935.80
10		86 902.1	87 018.5	86 765.91	86 849.27	86 964.28
11	86 851.7	86 939.8[e]	87 053.9	86 795.70	86 882.30	86 995.85
12		86 974.7	87 092.2	86 828.46	86 913.87	87 029.87
13			87 134.3	86 863.84	86 953.16	87 067.35
14			87 178.8	86 901.86	86 989.81	87 106.88
15			87 227.5	86 943.02	87 035.24	87 150.34
16			87 278.0	86 986.15	87 077.04	87 195.30
17			87 333.6[d]	87 033.08[d]	87 128.67	87 244.74
18			87 390.1	87 081.43[d]	87 175.57	87 295.08
19			87 452.6	87 134.28[d]	87 233.05[d]	87 350.60
20						87 406.27
21			87 584.5	87 246.37[d]		87 467.85
22			87 652.1[e]		87 406.13	87 528.79
23				87 369.28		87 596.49
24			87 801.9[e]			87 662.61
25						87 736.56
26			87 964.8[e]			
27						87 888.06
29						88 050.72

[a]Term values are referred to energy zeros defined by the hypothetical levels $X\,^3\Sigma_g^-(v=0,J=N=0,F_2)$, respectively, for each isotopomer. Ground-state terms used were from Ref. 25, for $^{16}O_2$, and Ref. 12, for $^{18}O_2$.
[b]Apparent linewidths $\gtrsim$1.6 cm^{-1} FWHM; calibration uncertainty ~0.2 cm^{-1}; relative uncertainties in terms from isolated lines 0.2–0.5 cm^{-1}.
[c]Apparent linewidths ~0.2–0.6 cm^{-1} FWHM; calibration uncertainty ~0.2 cm^{-1}; relative uncertainties in terms from isolated lines $\lesssim$0.1 cm^{-1}.
[d]Term value from shoulder(s) in spectrum.
[e]Term value from blended feature(s) in spectrum.

state involving the bound $\pi_g np\pi_u\ ^3\Sigma_u^-$ Rydberg states with $n=3$ and 4, and the repulsive $\pi_u^3\pi_g^3\ ^3\Sigma_u^-$ valence state, but, in contrast to the case for the $^3\Pi_u$ states, the MO configurations for these Rydberg and valence states differ by two orbitals. Nevertheless, there remain strong Rydberg-valence interactions, as mentioned in Sec. I. Diabatic and corresponding adiabatic potential-energy curves for the interacting $^3\Sigma_u^-$ states are shown in Fig. 2. The lower adiabatic curve in Fig. 2 can be associated with the well-known $B\,^3\Sigma_u^-$ state of O_2, while the upper adiabatic curve can be associated with the E state of interest here, the $E(v=3)$ level predicted to lie close to the $F(v=1)$ level. However, it should be noted that the adiabaticity parameter for the lowest $^3\Sigma_u^-$ Rydberg-valence crossing is $\zeta\approx1.3$, implying character intermediate between adiabatic and diabatic for the E-state levels in this region, i.e., the coupled-state energy levels will not closely coincide with the eigenenergies of the adiabatic E state of Fig. 2. This intermediate Rydberg-valence coupling is well known to produce very strong predissociation of the E-state levels by the B-state continuum.[4] Once again, however, it is necessary to use CSE methods to accurately treat this predissociation.

We employ a basic three-state diabatic CSE model similar to that of Ref. 13, but with slightly modified parameters, to describe the interacting $^3\Sigma_u^-$ states. In this model,[21] the diabatic Rydberg and valence $^3\Sigma_u^-$ potential-energy curves are those shown in Fig. 2, the Rydberg-valence couplings are 4037 and 2011 cm^{-1}, respectively, for the $3p\pi_u$ and $4p\pi_u$ states, and the diabatic $^3\Sigma_u^-\leftarrow X\,^3\Sigma_g^-$ electronic transition moments are taken from Ref. 13. Cross sections for excitation into the coupled $^3\Sigma_u^-$ states of isotopic O_2 were calculated in the energy range of the $F\leftarrow X(1,0)$ band using these model parameters and the CSE method described above.

Finally, the separate three-state models for the coupled $^3\Pi_u$ and $^3\Sigma_u^-$ states were combined together into a six-state model in an effort to explain rotational aspects of the $F(v=1)$-state predissociation. This was accomplished simply by including the **L**-uncoupling interactions expected to occur between the $np\sigma_u$ and $np\pi_u$ members of an np Rydberg

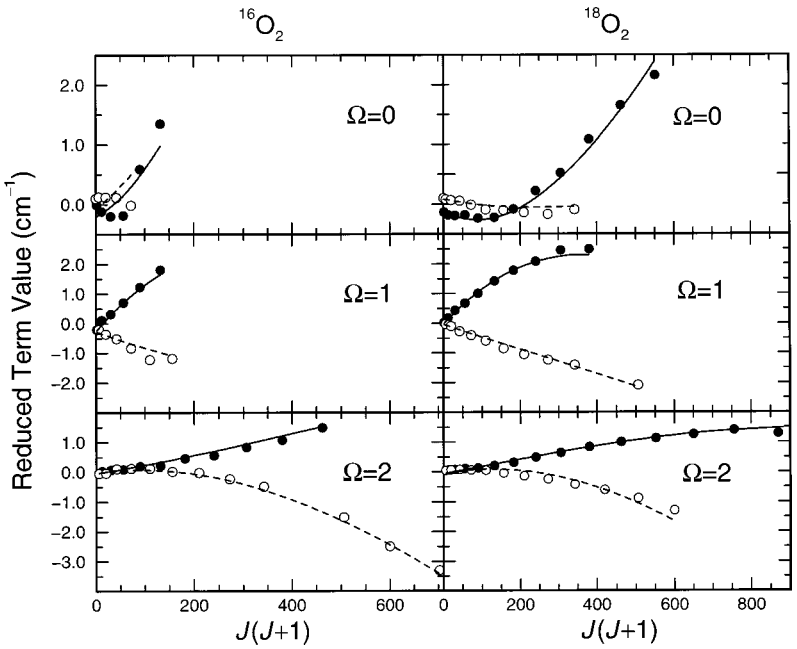

FIG. 4. Experimental reduced term values (see text) for the $F\,^3\Pi_{u\Omega}(v=1,J)$ levels of isotopic O_2, emphasizing Λ doubling. Solid circles: *e* levels. Open circles: *f* levels. Results of a fit to the $^3\Pi$ Hamiltonian of Brown and Merer (Ref. 26) are also shown. Solid curves: *e* levels. Dashed curves: *f* levels.

complex[1] as off-diagonal elements in the potential matrix. Specifically, these rotation and e/f-parity-dependent rotronic matrix elements are[22]

$$\langle {}^3\Pi_{u0},J,f^e|\mathbf{H}^{JL}|{}^3\Sigma^-_{u1},J,f^e\rangle = \mp\frac{1}{2\mu R^2}\sqrt{2J(J+1)},$$

$$\langle {}^3\Pi_{u1},J,e|\mathbf{H}^{JL}|{}^3\Sigma^-_{u0},J,e\rangle = -\frac{1}{\mu R^2}\sqrt{J(J+1)}, \qquad (3)$$

$$\langle {}^3\Pi_{u2},J,f^e|\mathbf{H}^{JL}|{}^3\Sigma^-_{u1},J,f^e\rangle = -\frac{1}{2\mu R^2}\sqrt{2J(J+1)},$$

where $\mathbf{H}^{JL}=-\mathbf{J}^-\mathbf{L}^+/(2\mu R^2)$. In the picture described by this model, the *F*-state predissociation is caused by a combination of a direct nonadiabatic mechanism involving predissociation by the $^3\Pi_u$ valence state, together with an indirect rotational mechanism involving predissociation by the $^3\Sigma^-_u$ valence state. Cross sections computed using this full six-state CSE model were used to determine predissociation linewidths for comparison with the experimental values in Sec. IV B.

IV. RESULTS AND DISCUSSION

Room-temperature photoabsorption cross sections for the $F\leftarrow X(1,0)$ bands of $^{16}O_2$ and $^{18}O_2$ are shown in Fig. 3. The spectrum for the heavier isotopomer is a composite of many individual, overlapping étalon scans. The resolution of neither spectrum in Fig. 3 is significantly limited by instrumental effects. Thus, it is immediately apparent that the rotational lines for $^{18}O_2$ are much narrower than those for $^{16}O_2$, implying a much lower rate of predissociation for $F(v=1)$ in the heavier isotopomer. Such a strong isotopic dependence is unusual for a low-vibrational level. Consequently, it is confirmed that apparent intensity anomalies observed previously in low-resolution studies of this band[6] were indeed caused by the well-known problems of determining the intensities of very narrow lines using inadequate instrumental resolution.

A. Structure

The subband and rotational-branch structures observed in Fig. 3 are consistent with expectation for a $^3\Pi_u$(regular) $\leftarrow{}^3\Sigma^-_g$ transition. For each isotopomer, however, the central ($\Omega'=1$) subband is significantly off-center, corresponding to a downward shift in energy of $F\,^3\Pi_{u1}$ by $\sim$20 cm^{-1}. It has been shown in detail elsewhere,[23] for $^{16}O_2$, that this effect is due to spin–orbit interaction with the $h\,^1\Pi_{u1}(v=0)$ state, which lies $\sim$370 cm^{-1} higher in energy. In the case of $^{18}O_2$, all 27 rotational branches expected for a $^3\Pi \leftarrow{}^3\Sigma$ transition were observed in either the room- or LN_2-temperature spectra. In the case of $^{16}O_2$, despite more severe line blending, only six branches (P_1, $^PQ_{12}$, $^PR_{13}$, P_2, Q_2, and R_2) remained unseen.

We have performed full assignments of the $F\leftarrow X(1,0)$ rotational structure for both isotopomers, employing both the room- and LN_2-temperature spectra.[24] The experimental wave numbers were combined with ground-state rotational terms (Veseth and Lofthus[25] for $^{16}O_2$, Steinbach and Gordy[12] for $^{18}O_2$) to determine term values for the $F(v=1)$ state. The results are given in Table I, referred to energy zeros defined by the hypothetical levels $X\,^3\Sigma^-_g(v=0,J=N=0,F_2)$, respectively, for each isotopomer. The tabulated terms represent averages obtained using as many branches as possible, with an emphasis on unblended lines.

Reduced term values, obtained from Table I by subtracting appropriate linear functions of $J(J+1)$, so as to emphasize the significant Λ doubling, are shown in Fig. 4. At low values of *J*, the behavior observed is characteristic of a $^3\Pi$ state close to Hund's case (a), with energy differences between the *e* levels (odd *J*, solid circles in Fig. 4) and the *f* levels (even *J*, open circles) approximately constant, for Ω

TABLE II. Fitted spectroscopic parameters for the $F\,^3\Pi_u(v=1)$ state of isotopic O_2, in cm^{-1}.

	$^{16}O_2$	$^{18}O_2$
ν_0[a]	86 740.23(11)[b]	86 705.30(9)
B	1.5663(16)	1.4010(12)
$D\times10^6$	0.0[c]	1.9(19)
A	98.01(11)	98.07(8)
λ	10.25(11)	9.89(8)
γ	0.12(6)	0.12(3)
A_D	0.0	−0.0026(12)
λ_D	0.0	0.0
$o+p+q$	0.05	0.10
$p+2q$	−0.05(7)	−0.034(9)
q	−0.022(4)	−0.0166(10)

[a]Experimental terms of Table I were fitted to the $^3\Pi$ Hamiltonian of Ref. 26 (zero-energy references as in footnote a of Table I).
[b]3σ uncertainties of the fit are given in parentheses, in units of the last-quoted decimal place. Origin uncertainty does not include absolute calibration uncertainty.
[c]Parameters without uncertainties fixed during fit.

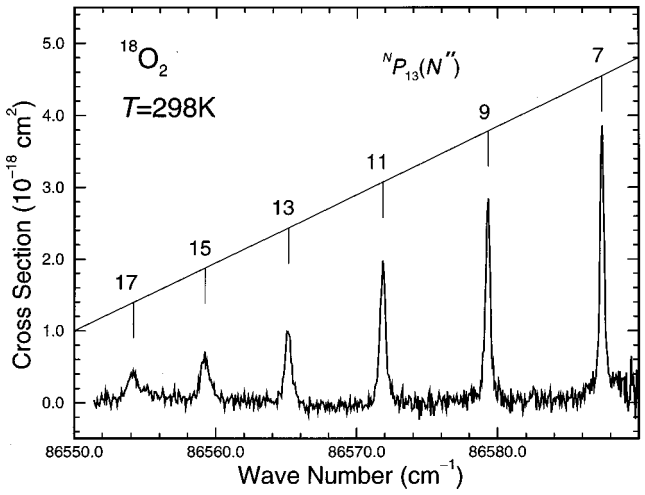

FIG. 5. A portion of the $^NP_{13}$ branch in the $F\,^3\Pi_{u0}\leftarrow X\,^3\Sigma_g^-(1,0)$ subband of $^{18}O_2$, at room temperature, demonstrating a significant increase in linewidth with increasing rotational quantum number.

$=0$, and with quadratic and quartic dependences on J, for $\Omega=1$ and 2, respectively.[26] However, for increasing J values, there are rapid deviations from this behavior.

We have least-squares fitted the terms in Table I to the $^3\Pi$ Hamiltonian of Brown and Merer,[26] obtaining the spectroscopic parameters listed in Table II. The corresponding fitted (reduced) term values for the e and f levels are shown in Fig. 4 as solid and dashed curves, respectively, and are compared with the experimental values. Where the relative uncertainty in a fitted parameter was excessively large, that parameter was held fixed during the final fitting procedure. Because of the restricted range of rotational levels observed in the $\Omega=0$ and 1 sublevels of $^{16}O_2$, for example, no centrifugal-distortion parameters could be determined. The quality of fit obtained was good for both isotopomers, with root-mean-square deviations of 0.15 and 0.10 cm^{-1}, respectively, for $^{16}O_2$ and $^{18}O_2$. Nevertheless, there remained some *systematic* discrepancies for each isotopomer, especially in the $\Omega=0$ sublevel of $^{16}O_2$. These discrepancies tended to skew the fitted value of the Λ-doubling parameter $o+p+q$, so this parameter was fixed during the final fits at a nonzero value determined by the low-rotation e-f splitting for $\Omega=0$. Since the Brown and Merer[26] Hamiltonian is expected to fail only in the case of perturbation by a close-lying state, the residual systematic discrepancies observed here suggest a possible perturbation, which is strongest in the case of the $\Omega=0$ sublevel of $^{16}O_2$.

The anomalous nature of the F state, apparent in its vibrational splittings,[6] is supported by the principal spectroscopic parameters determined here and shown in Table II. For example, the fitted origins imply an isotopic shift of 34.9 cm^{-1}, much smaller than expected for a $v=1$ level, while the ratio[27] of isotopic rotational constants $B^r=B^{18}/B^{16}=0.8945(12)$ differs significantly from the value expected for a well-behaved state, i.e., the ratio of the reduced masses for the two isotopomers, $\mu^{16}/\mu^{18}=0.8886$.[28] The main reason for this behavior derives from the strongly mixed nature of the $F(v=1)$ level, described in Sec. III. Inspection of Fig. 1 shows that $F(v=1)$ should have significant $4p\sigma_u\,^3\Pi_u(v=0)$ character, helping to explain the low value of the isotopic shift. The close similarity observed between the fitted isotopic values of the diagonal spin–orbit constant A, despite this mixing, can be explained by noting that the mixed states are expected to have similar, isotopically independent values of $A=a_{\pi_g}$, where a_{π_g} is a molecular spin–orbit parameter[1] determined by their common π_g MO. Finally, we note that the fitted values of λ reflect primarily the $F\,^3\Pi_{u1}(v=1)\sim h\,^1\Pi_{u1}(v=0)$ spin–orbit perturbation described above,[29] the slightly larger value for $^{16}O_2$ arising probably due to the smaller difference in energy between the perturbing levels.

B. Predissociation

In addition to the much lower overall degree of predissociation for the heavier isotopomer implied by the relative linewidths in Fig. 3, two further conclusions regarding details of the predissociation of $F(v=1)$ follow from a close examination of the spectra. First, some branches exhibit a significant increase in linewidth with increasing rotational quantum number. This effect is readily apparent, for example, in Fig. 5, in which a portion of the $^NP_{13}$ branch from the $\Omega'=0$ subband of $^{18}O_2$ at room temperature is shown in detail.[30] Second, for both isotopomers, but more easily seen in $^{16}O_2$, rotational transitions terminating on $\Omega=1(e)$ levels of the F state broaden much more rapidly with increasing rotation than do those terminating on the corresponding $\Omega=1(f)$ levels. This effect is illustrated clearly in the LN_2-temperature spectrum of $^{16}O_2$ shown in Fig. 6, where the $^SR_{21}(5)$ line, terminating on the $\Omega=1$, $J=7$, e-parity level, is much broader than the $^RQ_{21}(9)$ line, which terminates on the $\Omega=1$, $J=10$, f-parity level.

In order to obtain a complete picture of the $F(v=1)$-state predissociation, we have performed a detailed linewidth analysis on the room- and LN_2-temperature spectra for both isotopomers. Segments of the experimental cross sections were least-squares fitted to synthetic cross sections in which each rotational line was represented by a Voigt profile. The line centers, strengths, and Lorentzian (predisso-

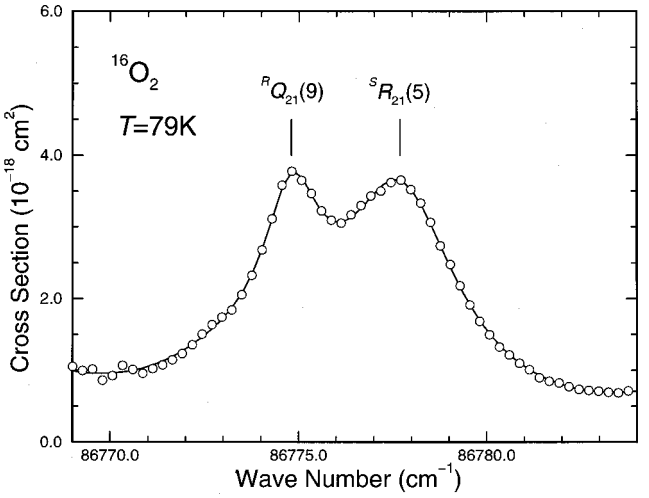

FIG. 6. Narrow region in the $F\,^3\Pi_{u1} \leftarrow X\,^3\Sigma_g^-(1,0)$ subband of $^{16}O_2$, at LN_2 temperature, highlighting the e/f-parity dependence of linewidth for this subband. Open circles: experimental photoabsorption cross section. Solid curve: model cross-section fit. The fitted Lorentzian width of the $^RQ_{21}(9)$ line, corresponding to an upper-state $J=10$, f-parity level, is 1.8 cm^{-1} FWHM, less than half of the value 3.8 cm^{-1} FWHM for the $^SR_{21}(5)$ line, corresponding to an upper-state $J=7$, e-parity level.

TABLE III. Experimental predissociation widths for the $F\,^3\Pi_{u\Omega}(v=1,J)$ levels of isotopic O_2, in cm^{-1} FWHM.

	$^{16}O_2$			$^{18}O_2$		
J	$\Omega=0$	$\Omega=1$	$\Omega=2$	$\Omega=0$	$\Omega=1$	$\Omega=2$
0	2.28(48)[a]			0.01(13)		
1					0.06(4)	
2	2.04(30)	1.61(23)	1.58(24)	0.00(7)	0.06(3)	0.05(4)
3			1.56(14)	0.02(3)	0.05(2)	0.03(2)
4		1.58(22)	1.96(37)	0.03(10)	0.09(4)	0.13(6)
5	2.68(14)	2.92(46)		0.06(3)	0.11(5)	0.02(2)
6		1.65(15)		0.09(6)	0.11(2)	0.19(8)
7	4.34(51)	3.82(19)		0.18(4)	0.14(4)	0.03(2)
8		1.68(30)		0.17(2)	0.09(3)	0.15(3)
9	6.16(279)	5.23(41)	1.80(7)	0.28(5)	0.16(4)	0.25(4)
10		1.80(12)		0.25(4)	0.14(4)	0.20(3)
11			2.14(16)	0.37(8)	0.20(7)	
12			2.75(26)	0.34(7)	0.13(4)	0.24(3)
13			2.25(23)	0.47(13)	0.23(7)	0.19(3)
14				0.46(18)	0.18(5)	0.22(3)
15			2.90(67)	0.41(15)	0.38(10)	0.08(2)
16					0.24(7)	0.27(7)
17					0.41(17)	0.21(5)
18					0.20(6)	0.31(6)
20						0.28(3)
21						0.28(12)
23				0.61(28)		0.26(12)

[a]3σ uncertainties are given in parentheses, in units of the last-quoted decimal place.

ciation) width components Γ_L were allowed to vary freely in the fitting procedure, while the Gaussian width component was held fixed at the appropriate Doppler width (~0.19 cm^{-1} FWHM at 298 K, ~0.10 cm^{-1} FWHM at 79 K). The background cross sections were fitted by a low-order polynomial in energy and instrumental effects were allowed for by convolution (in transmission) with a Gaussian of 0.15 cm^{-1} FWHM.[31] The results of a typical fitting procedure are shown in Fig. 6, where the fit (solid curve) is seen to accurately reproduce the experimental cross section (open circles).

The final results of the predissociation-width analysis are summarized in Table III and illustrated in Fig. 7. Each width entry in Table III represents a weighted average of separate results for all analyzable lines terminating on the given upper-state level, preference being given to results from unblended lines, where possible. The general observations mentioned previously are confirmed by the detailed analysis. First, the predissociation widths for $^{16}O_2$ greatly exceed those for $^{18}O_2$. Second, for $^{16}O_2$, the $\Omega=0$ and $\Omega=1(e)$ widths increase rapidly with increasing rotation, while the $\Omega=2$ widths increase less rapidly and the $\Omega=1(f)$ widths hardly at all. Similar behavior is observed for $^{18}O_2$, but in this case there is an underlying parity-independent J dependence of the $\Omega=1(f)$ and $\Omega=2$ widths (and, possibly, the other Ω components), which is of significantly greater relative magnitude than is the case for $^{16}O_2$, making the e-f width dependence for $\Omega=1$ more difficult to detect.

In order to determine the rotationless predissociation widths Γ_0 for the various isotopic sublevels, we have fitted low-order polynomials of the form $\Gamma_L(J)=\Gamma_0+\Gamma_J J(J+1)+\ldots$ to the experimental widths. The order of the polynomial varied from linear, for $^{16}O_2$ where the accessible range of J is restricted, to cubic, for the $\Omega=0$ and 2 sublevels of $^{18}O_2$. The results, listed in Table IV, show that there is no statistically significant sublevel dependence of Γ_0, and yield Ω-averaged values of 1.56(6) cm^{-1} FWHM and 0.03(3) cm^{-1} FWHM, respectively, for $^{16}O_2$ and $^{18}O_2$, corresponding to an isotopic width ratio $\Gamma_0^r=\Gamma_0^{18}/\Gamma_0^{16}=0.019(19)$. This is a startlingly strong isotopic effect. In the case of the $E\,^3\Sigma_u^-(v=0)$ state of O_2, another example of anomalous isotopic predissociation, the corresponding width ratio is 0.30 (0.16 for $^{16}O\,^{18}O$).[4] The present anomalous isotopic effect comes from the class of *nonadiabatic predissociation*, discussed by Lefebvre-Brion and Field,[1] and illustrated by examples in the $C\,^2\Sigma_u^+(v\geqslant 3)$ state of N_2^+ where width ratios $\Gamma^r=\Gamma^{15}/\Gamma^{14}\approx 0.1$ occur.[32] As discussed in Sec. III, in an adiabatic picture (solid curves in Fig. 1), the F-state predissociation occurs through residual nonadiabatic interactions and, as demonstrated in detail by Lefebvre-Brion and Field,[1] strong isotopic effects can occur in this type of predissociation. Using the CSE model of the $^3\Pi_u$ Rydberg-valence interactions described in Sec. III, we have computed $F(v=1)$ rotationless predissociation widths, also listed in Table IV, of 1.2 cm^{-1} FWHM and 0.006 cm^{-1} FWHM, respectively, for $^{16}O_2$ and $^{18}O_2$, corresponding to a width ratio $\Gamma_0^r=0.005$. These computed values are in satisfactory agreement with experiment, especially considering that the $^3\Pi_u$ CSE model described in Sec. III and employed here has been optimized by fitting to a wide range of spectroscopic data covering a significant energy range,[13] with no special weighting in favor of the $F(v=1)$ level which is the subject of this work.

While, as we have shown, the rotationless isotopic $F(v=1)$ widths can be explained in terms of a nonadiabatic predissociation mechanism involving only the Rydberg and

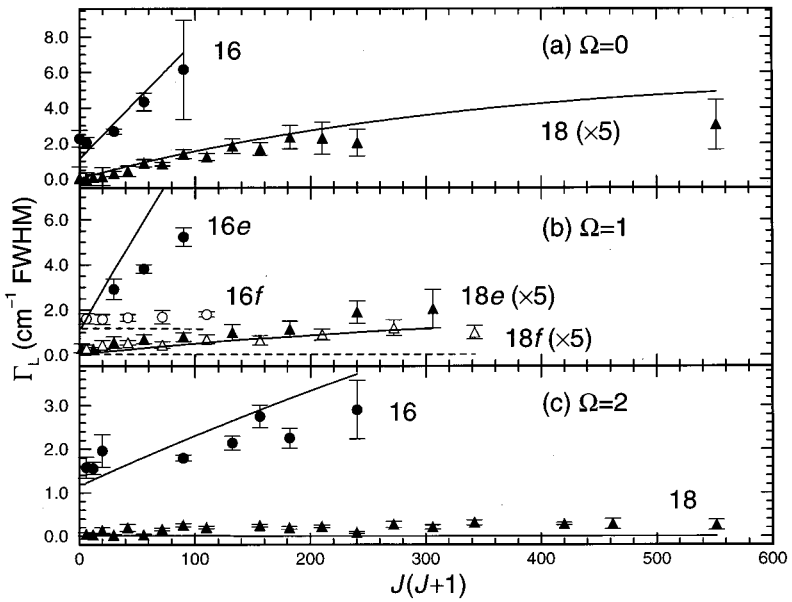

FIG. 7. Isotopic predissociation widths for the $F\,^3\Pi_{u\Omega}(v=1,J,e/f)$ levels of O_2. Circles: Experimental widths for $^{16}O_2$. Triangles: Experimental widths for $^{18}O_2$. Curves: Computed CSE model widths. (a) $\Omega=0$. No e/f-parity dependence. (b) $\Omega=1$. Solid symbols and curves: e parity. Open symbols and dashed curves: f parity. (c) $\Omega=2$. No e/f-parity dependence.

valence states of $^3\Pi_u$ symmetry, such a mechanism predicts no significant variation of width with rotation, e/f parity, or sublevel component. Since, for nonzero J, the experimental widths in Fig. 7 exhibit significant dependencies on these parameters, another predissociation mechanism must be found to explain the rotational broadening. The clue to this explanation lies in the dramatic difference in rotational broadening (especially for $^{16}O_2$) observed between the e and f levels of the $\Omega=1$ component [see Fig. 7(b)]. According to the selection rules for perturbations,[1] only a $^3\Sigma^-_{u0}$ (e-parity) state can selectively perturb $^3\Pi_{u1}(e)$ levels, through a J-dependent **L**-uncoupling interaction.[33] Thus, it is certain that the rotational broadening of the $F\,^3\Pi_{u1}(v=1,e)$ levels is caused by an **L**-uncoupling interaction with a (pre)dissociative $^3\Sigma^-_{u0}$ state. Analogous interactions between the $^3\Sigma^-_{u1}$ and $^3\Pi_{u0,2}$ sublevels will produce a degree of non-parity-dependent rotational broadening in the $F\,^3\Pi_{u0,2}(v=1)$ sublevels.

TABLE IV. Comparison between experimental and computed CSE model $F\,^3\Pi_u(v=1)$ predissociation widths for isotopic O_2. Both the experimental and computed Lorentzian linewidths were fitted to polynomials of the form: $\Gamma_L(J)=\Gamma_0+\Gamma_J J(J+1)+\cdots$. The rotationless and rotation-dependent widths, Γ_0 and Γ_J, respectively, are in cm^{-1} FWHM.

		Γ_0		Γ_J	
Iso.	$\Omega(^e_f)$	Expt.	Calc.	Expt.	Calc.
$^{16}O_2$	0	1.8(9)[a]	1.2	0.040(2)[b]	0.062
	1(e)	1.7(5)	1.2	0.041(2)[b]	0.084
	1(f)	1.56(6)	1.2	0.0021(6)[b]	0.0000
	2	1.5(4)	1.2	0.004(2)[b]	0.012
$^{18}O_2$	0	0.00(3)[c]	0.006	0.0030(7)	0.0034
	1(e)	0.04(4)	0.006	0.0014(10)	0.0011
	1(f)	0.07(5)	0.006	0.0006(8)	0.0000
	2	0.03(10)	0.006	0.0009(13)	0.0000

[a]3σ uncertainties are given in parentheses, in units of the last-quoted decimal place.
[b]Γ_0 fixed at 1.56 cm^{-1} FWHM during fitting procedure.
[c]The fitted intercept was $-0.02(5)$ cm^{-1} FWHM.

Using the CSE model of the $^3\Sigma^-_u$ Rydberg-valence interactions described in Sec. III, we have computed the rotationless $^3\Sigma^-_u \leftarrow X\,^3\Sigma^-_g$ cross sections in the region of the $F \leftarrow X(1,0)$ band, for each isotopomer. The results are compared in Fig. 8 with experimental LN_2-temperature total photoabsorption cross sections.[34] In the case of $^{16}O_2$, the CSE calculations predict a weak, broad predissociating resonance, lying between the $\Omega'=0$ and 1 subbands of the $F \leftarrow X(1,0)$ transition, which is associated with the transition into the $E\,^3\Sigma^-_u(v=3)$ state. For this isotopomer, there is some circumstantial evidence for the accuracy of the calculations in the shape of the high-energy wing in the experimental cross section, but it is not possible to unambiguously detect the $E \leftarrow X(3,0)$ transition directly due to the overlap with $F \leftarrow X(1,0)$. On the other hand, while the calculated $^3\Sigma^-_u \leftarrow X\,^3\Sigma^-_g$ cross section for $^{18}O_2$ in Fig. 8 predicts a significantly weaker resonance than that for $^{16}O_2$, the different isotopic shift of the $F \leftarrow X(1,0)$ band results in the $E \leftarrow X(3,0)$ band being visible in the experimental cross section as a weak, broad feature near 86 530 cm^{-1} on the low-energy wing of $F \leftarrow X(1,0)$. This represents the first experimental observation of a transition into the $E(v=3)$ level of O_2 and serves to confirm the reliability of the CSE calculations for the $^3\Sigma^-_u$ states. The extreme weakness of the $E \leftarrow X(3,0)$ band for each isotopomer is due to a destructive interference effect between the Rydberg and valence transition amplitudes, an effect first predicted and discussed in Ref. 13. The computed positions of the isotopic $E \leftarrow X(3,0)$ bands in Fig. 8 qualitatively support the observed pattern of $F(v=1)$ rotational broadening, the closer $F(v=1) \sim E(v=3)$ coincidence in energy for $^{16}O_2$ leading to greater broadening, and their location on the low-energy side of $F \leftarrow X(1,0)$ leading to a lesser degree of broadening for the $\Omega=2$ components of each isotope.

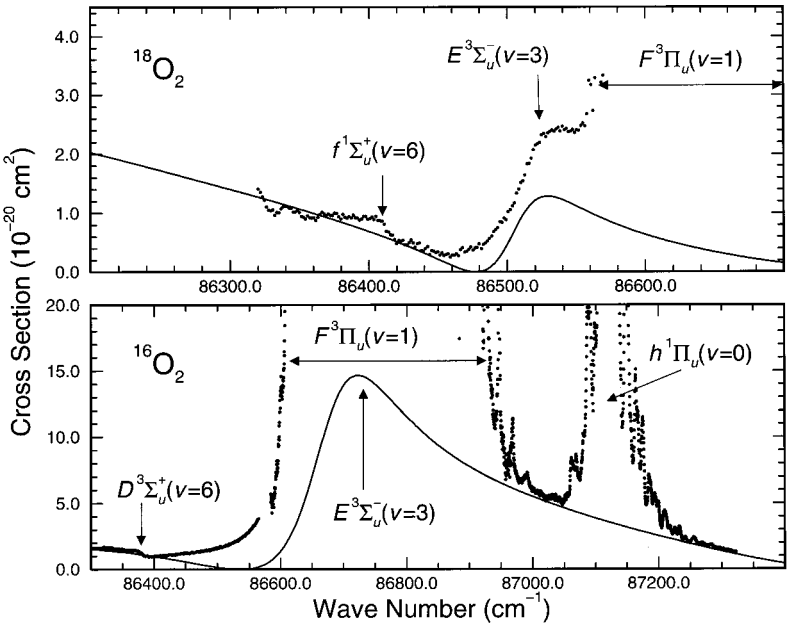

FIG. 8. Photoabsorption cross sections in the wings of the $F\,^3\Pi_u \leftarrow X\,^3\Sigma_g^-(1,0)$ band of isotopic O_2. Solid circles: experimental LN_2-temperature cross sections. Solid curves: computed CSE rotationless cross sections for the underlying $^3\Sigma_u^- \leftarrow X\,^3\Sigma_g^-$ transitions. Spectral features are labeled according to the upper states of the corresponding transitions. Evidence for the $E\,^3\Sigma_u^-(v=3)$ state, suggested herein to be responsible for the rotational predissociation of $F\,^3\Pi_u(v=1)$, is provided by good agreement between the underlying experimental and computed cross sections in the high-energy wing for $^{16}O_2$, and also, most clearly, by the observation of a weak peak, near 86 530 cm^{-1}, in the low-energy wing for $^{18}O_2$.

Using the combined, six-state $^3\Pi_u \sim ^3\Sigma_u^-$ CSE model, with the **L**-uncoupling interaction matrix elements given in Eq. (3), we have computed isotopic predissociation widths for $F(v=1)$ as functions of rotation, e/f parity, and Ω sublevel. The results, also shown in Fig. 7, are in reasonable overall agreement with the experimental values and reproduce all of the principal dependencies described above. Detailed comparison is made between the computed and experimental low-rotational linear slopes Γ_J in Table IV, where it is seen that the computed values exceed the experimental values significantly for $^{16}O_2$, $\Omega=0$, $1(e)$, and 2, but are in quite good agreement for $^{18}O_2$, $\Omega=0$ and 1 $(e-f$ difference). The greater discrepancies for $^{16}O_2$ are probably related to the closer energy degeneracy between $F(v=1)$ and $E(v=3)$ for this isotopomer. In this case, the results will be not only highly sensitive to the exact position of the $E(v=3)$ perturber, but also to the *shape* of its broad profile. Since this resonance cannot be observed directly for $^{16}O_2$, it is difficult to optimize its characteristics in the CSE model. Regardless of these discrepancies in detail, it is clear that the major aspects of the variations in width with rotation, e/f parity, and Ω sublevel are due to an *indirect* (accidental) predissociation involving **L**-uncoupling interactions between $F(v=1)$ and the $E(v=3)$ predissociating resonance. Nevertheless, there remain minor effects that cannot be explained by this mechanism, in particular, the residual increases in width with rotation for $^{16}O_2$, $\Omega=1(f)$, and $^{18}O_2$, $\Omega=1(f)$ and 2. Further **L**-uncoupling interactions between $F(v=1)$ and predissociated levels of the $^3\Delta_u$ components of the *np* Rydberg complexes, which certainly exist in this region of energy, may provide an explanation for the remaining minor rotational predissociation.

The same $F(v=1)\sim E(v=3)$ **L**-uncoupling interaction proposed as the cause of the major rotational predissociation of $F(v=1)$ should also result in perturbations in the effective rotational constants of the $F(v=1)$ sublevels. In particular, this effect should be most readily observable as a perturbation in $\Delta B_{ef}=B_e-B_f$ for the $\Omega=1$ sublevel, since the f levels will remain unperturbed by the interaction, but the e levels will be shifted to higher energies, increasingly as J increases, by the lower-lying $E(v=3)$ state. The experimental $\Omega=1$ terms shown in Fig. 4 yield effective values of $\Delta B_{ef}=0.025(2)$ and $0.017(1)$ cm^{-1}, respectively, for $^{16}O_2$ and $^{18}O_2$, consistent with a stronger perturbation in the case of $^{16}O_2$ where the $F(v=1)$ and $E(v=3)$ levels are in closer proximity. Calculations performed using the combined $^3\Pi_u \sim ^3\Sigma_u^-$ CSE model of Sec. III imply perturbations in ΔB_{ef} of 0.036 and 0.015 cm^{-1}, respectively, for $^{16}O_2$ and $^{18}O_2$, caused by the **L**-uncoupling interaction. As in the case of the rotational predissociation discussed above, the calculations exceed the experimental result for $^{16}O_2$, but are in good agreement for $^{18}O_2$. Nevertheless, it is clear that both the major rotational predissociation of $F(v=1)$, and the parity-dependent perturbation of the $\Omega=1$ sublevel, are consistent with a single cause, namely the $F(v=1)\sim E(v=3)$ **L**-uncoupling interaction. In addition, the CSE calculations suggest that most, if not all, of the observed Λ doubling for the $\Omega=1$ sublevel is directly attributable to the same interaction.

Experiments in which the $O(^1D)$ quantum yield in the photodissociation of O_2 is measured enable photodissociation branching ratios to be inferred, allowing further testing of our suggested predissociation mechanisms for the $F(v=1)$ state. Gibson and Lewis[35] and Lee and Nee[36] measured integrated $O(^1D)$ quantum yields of 0.41(8) and 0.38, respectively, over the region of the $F \leftarrow X(1,0)$ band of $^{16}O_2$. The nonadiabatic mechanism proposed here to explain the rotationless predissociation of $F(v=1)$, involving $^3\Pi_u$ Rydberg-valence interactions, results in $O(^3P)+O(^3P)$ dissociation products (see Fig. 1). However, the indirect mechanism proposed to explain the major rotational predissociation, involving $^3\Sigma_u^-$ Rydberg-valence-coupled states, results in $O(^1D)+O(^3P)$ dissociation products (see Fig. 2). Thus, a comparison between the rotational and rotationless predissociation rates $(\propto\Gamma_L)$ will result in a prediction of the $O(^1D)$

$+O(^3P)$ predissociation branching ratio, equivalent to the experimental $O(^1D)$ quantum yield.[37] At room temperature, the most probable ground-state rotational level populated is $N'' \approx 9$. If we take $J=9$, $\Gamma_0 = 1.56\ cm^{-1}$ FWHM, and use the Γ_J values for $^{16}O_2$, $\Omega=0$, $1(e)$, and 2 from Table IV, we obtain $O(^1D)+O(^3P)$ predissociation branching ratios of 0.70, 0.70, 0.0, and 0.19, for the $\Omega=0$, $1(e)$, $1(f)$, and 2 sublevels, respectively, or a sublevel-averaged value of 0.41,[38] in good agreement with the experimental $O(^1D)$ quantum yield.[35,36] The calculated sublevel distribution of the $O(^1D)+O(^3P)$ predissociation branching ratio is also in agreement with the experimental observations which show the $O(^1D)$ signal peaking under the $\Omega'=0$ and 1 subbands.[35,36] Thus, independent experimental measurements of the $O(^1D)$ photodissociation quantum yield support both the present predissociation width analysis and the suggested rotationless and major rotational predissociation mechanisms. Elucidation of the minor rotational predissociation mechanisms, e.g., for $^{16}O_2$, $\Omega=1(f)$, and $^{18}O_2$, $\Omega=1(f)$ and 2, might, perhaps, be assisted by further measurements of the $O(^1D)$ quantum yield, for both isotopomers, over a wide range of temperatures, and with significantly higher instrumental resolution.

C. Oscillator strength

Using the relationship $f = 1.13\times10^{12} \int \sigma(\nu) d\nu$, and integrating over the $F \leftarrow X(1,0)$ room-temperature band cross sections, we obtain the experimental oscillator strengths $f^{16} = 1.37(5)\times10^{-3}$ and $f^{18} = 1.11(10)\times10^{-3}$.[39] The oscillator strength for $^{16}O_2$ has been corrected downwards by 3.5%, to allow for the computed contribution from the coincident $E \leftarrow X(3,0)$ transition (see Fig. 8). These values are in good agreement with those calculated using the rotationless three-state $^3\Pi_u$ CSE model, $f^{16}=1.26\times10^{-3}$ and $f^{18}=1.14\times10^{-3}$, both the experimental and calculated oscillator strengths implying a significant isotope effect.

V. SUMMARY AND CONCLUSIONS

Using a tunable, narrow-bandwidth vacuum-ultraviolet source based on third-harmonic generation from excimer-pumped dye-laser radiation, the $F\,^3\Pi_u \leftarrow X\,^3\Sigma_g^-(1,0)$ photoabsorption cross sections of $^{16}O_2$ and $^{18}O_2$ have been recorded in high resolution. Rotational analyses have been performed and the resultant $F(v=1)$ term values fitted to the $^3\Pi$ Hamiltonian of Brown and Merer.[26]

An extraordinarily large rotationless isotope effect is observed in the $F(v=1)$ predissociation, wherein the Lorentzian linewidth components for $^{18}O_2$ are a factor of $\sim$50 smaller than the corresponding $^{18}O_2$ linewidths. This effect, a consequence of the nonadiabatic rotationless predissociation mechanism, is described using a coupled-channel treatment of the strongly Rydberg-valence-mixed $^3\Pi_u$ states.

Significant J, e/f-parity, and sublevel dependencies observed in the isotopic $F(v=1)$ rotational widths are found to derive from an indirect predissociation mechanism involving an accidental degeneracy with the $E\,^3\Sigma_u^-(v=3)$ level, itself strongly predissociated by $^3\Sigma_u^-$ Rydberg-valence interactions, together with **L**-uncoupling (rotational) interactions between the Rydberg components of the F and E states. Transitions into the $E(v=3)$ level are observed directly for the first time, specifically in the $^{18}O_2$ spectrum.

These proposed rotationless and major rotational predissociation mechanisms are consistent with independent experimental measurements of the $F(v=1)$ predissociation branching ratios.[35,36] However, further investigations are required to elucidate the mechanism for minor residual $F(v=1)$ rotational predissociation (maximum linewidths $\lesssim$0.3 cm^{-1} FWHM), possibly involving $^3\Delta_u$ states, which is inexplicable using the present coupled-channel model.

ACKNOWLEDGMENTS

The authors would like to thank Professor H. Lefebvre-Brion, for a critical reading of the manuscript, K. J. Lonsdale and C. J. Dedman for valuable technical assistance, and Dr. K. G. H. Baldwin for laser-system advice. Partial support was provided by an NSF International Opportunities for Scientists and Engineers Program Grant No. INT-9513350, and Visiting Fellowships for G.S. and J.B.W. at the Australian National University.

[1] H. Lefebvre-Brion and R. W. Field, *Perturbations in the Spectra of Diatomic Molecules* (Academic, Orlando, 1986), pp. 39, 51–58, 90–92, 208–211, 277–279, 368–372.
[2] B. R. Lewis, S. T. Gibson, S. S. Banerjee, and H. Lefebvre-Brion, J. Chem. Phys. **113**, 2214 (2000).
[3] M. Ogawa, Can. J. Phys. **53**, 2703 (1975).
[4] B. R. Lewis, S. T. Gibson, M. Emami, and J. H. Carver, J. Quant. Spectrosc. Radiat. Transf. **40**, 1 (1988).
[5] K. G. H. Baldwin, S. T. Gibson, B. R. Lewis, J. H. Carver, and T. J. McIlrath, in *Proceedings on Short-Wavelength Coherent Radiation*, edited by P. H. Bucksbaum and N. M. Ceglio (Optical Society of America, Washington, D.C., 1991), Vol. 11, p. 12.
[6] J. P. England, B. R. Lewis, S. T. Gibson, and M. L. Ginter, J. Chem. Phys. **104**, 2765 (1996).
[7] B. R. Lewis, S. T. Gibson, R. A. Copeland, and C. G. Bressler, Phys. Rev. Lett. **82**, 4212 (1999).
[8] R. Mahon, T. J. McIlrath, V. P. Myerscough, and D. W. Koopman, IEEE J. Quantum Electron. **15**, 444 (1979).
[9] G. Stark, B. R. Lewis, S. T. Gibson, and J. P. England, Astrophys. J. **505**, 452 (1998).
[10] G. Stark, B. R. Lewis, S. T. Gibson, and J. P. England, Astrophys. J. **520**, 732 (1999).
[11] M. Eidelsberg, J.-Y. Roncin, A. Le Floch, F. Launay, C. Leteltzer, and J. Rostas, J. Mol. Spectrosc. **121**, 309 (1987).
[12] W. Steinbach and W. Gordy, Phys. Rev. A **8**, 1753 (1973).
[13] B. R. Lewis, J. P. England, S. T. Gibson, M. J. Brunger, and M. Allan, Phys. Rev. A **63**, 022707 (2001).
[14] K. Dressler, Ann. Isr. Phys. Soc. **6**, 141 (1983).
[15] F. H. Mies, Mol. Phys. **41**, 953 (1980).
[16] E. F. van Dishoeck, M. C. van Hemert, A. C. Allison, and A. Dalgarno, J. Chem. Phys. **81**, 5709 (1984).
[17] L. Torop, D. G. McCoy, A. J. Blake, J. Wang, and T. Scholz, J. Quant. Spectrosc. Radiat. Transf. **38**, 9 (1987).
[18] B. R. Lewis, S. S. Banerjee, and S. T. Gibson, J. Chem. Phys. **102**, 6631 (1995).
[19] B. R. Johnson, J. Chem. Phys. **69**, 4678 (1978).
[20] P. C. Cosby (private communication).
[21] B. R. Lewis (unpublished).
[22] J. W. C. Johns and D. W. Lepard, J. Mol. Spectrosc. **55**, 374 (1975).
[23] J. P. England, B. R. Lewis, and M. L. Ginter, J. Chem. Phys. **103**, 1727 (1995).
[24] Full line lists are available from the authors.
[25] L. Veseth and A. Lofthus, Mol. Phys. **27**, 511 (1974).
[26] J. M. Brown and A. J. Merer, J. Mol. Spectrosc. **74**, 488 (1979).
[27] Throughout this work, 3σ uncertainties are given in parentheses, in units of the last-quoted decimal place.

[28] G. Herzberg, *Molecular Spectra and Molecular Structure, I. Spectra of Diatomic Molecules* (Van Nostrand, New York, 1950), pp. 141–145.
[29] The effective spin–spin parameter λ contains the effects of external interactions that produce an unequal splitting of the $^3\Pi$ sublevels.
[30] Note that only odd-N'' levels occur in the ground states of the homonuclear $^{16}O_2$ and $^{18}O_2$, due to nuclear-symmetry restrictions.
[31] Due to the high experimental resolving power, the instrument-function convolution was strictly necessary only for the very narrowest lines near the band heads for $^{18}O_2$.
[32] A. L. Roche and J. Tellinghuisen, Mol. Phys. **38**, 129 (1979).
[33] $^3\Sigma_{u0}^-$ states have no *f* levels.
[34] The experimental $^{18}O_2$ cross section and the low-energy part of the $^{16}O_2$ cross section in Fig. 8 are from lower-resolution monochromator measurements [J. P. England and B. R. Lewis (unpublished)].
[35] S. T. Gibson and B. R. Lewis, J. Electron Spectrosc. Relat. Phenom. **80**, 9 (1996); (unpublished).
[36] P. C. Lee and J. B. Nee, J. Chem. Phys. **112**, 1763 (2000).
[37] The $O(^1D)+O(^1D)$ dissociation channel is also open for $\lambda<1370$ Å, but this channel is not expected to contribute in the region of the $F\leftarrow X(1,0)$ band near 1153 Å.
[38] A complete analysis would require averaging over the entire rotational-branch structure of the $F\leftarrow X(1,0)$ band. This complexity is unwarranted in the present work.
[39] The finite instrumental resolving power has a negligible effect on the integrated cross sections and associated oscillator strengths.